Available online at www.sciencedirect.com
ScienceDirect
International Journal of Heat and Mass Transfer 51 (2008) 4911–4925
International Journal of HEAT and MASS TRANSFER
www.elsevier.com/locate/ijhmt

# Device scaling effect on the spectral-directional absorptance of wafer's front side

Kang Fu [a], Yu-Bin Chen [b], Pei-feng Hsu [a,*], Zhuomin M. Zhang [b], Paul J. Timans [c]

[a] *Mechanical and Aerospace Engineering Department, Florida Institute of Technology, Melbourne, FL 32901, USA*
[b] *George W. Woodruff School of Mechanical Engineering, Georgia Institute of Technology, Atlanta, GA 30332, USA*
[c] *Mattson Technology, Fremont, CA 94538, USA*

Received 7 March 2007; received in revised form 14 November 2007
Available online 21 April 2008

**Abstract**

Nonuniform absorption of thermal radiation in the rapid thermal processing of wafers is a critical problem facing the semiconductor industry. This paper presents a parametric study of the radiative properties of patterned wafers with the smallest feature dimension down to 10 nm, considering the effects of temperature, wavelength, and angle of incidence. Various gate and trench sizes and their dimensions relative to the period are used in examining the effect of device scaling on the spectral-directional absorptance via numerical solutions of the Maxwell equations. In the cases with trench size variation, the resonance cavity effect may increase the absorptance as the trench width increases. In the cases with trench size increases at several different filling ratios, the absorptance does not change much at small filling ratio. Wood's anomaly appears in the directional-hemispherical absorptance with gates on top of silicon substrate.


*Keywords:* Rapid thermal processing; Finite-difference time-domain; Rigorous coupled-wave analysis; Periodic nano-structures

## 1. Introduction

According to the International Technology Roadmap for Semiconductors [1], the gate length and junction depth of the 65-nm devices used in high-performance complementary metal oxide semiconductor (CMOS) technology will be 25 and 13.8 nm, respectively. Rapid thermal processing (RTP) currently provides the high-temperature annealing needed to create ultra-shallow junctions. However, the ion implantation annealing time, which ranges from 1 to 10 s above 1000 °C in conventional RTP, is too long to confine ion diffusion and achieve the implanted doping distribution within the junction. This difficulty can be overcome by using high-intensity flash-lamps or laser annealing with heating pulses lasting only a few milliseconds [2]. The typical energy sources are Ar or Xe arc lamps, which mainly emit ultraviolet and visible radiation. In flash-lamp heating, optical energy is absorbed at the wafer front side because of the small penetration depth that results from the large absorption coefficient of Si within the lamp spectrum.

Because the energy is absorbed within milliseconds, thermal diffusion cannot distribute heat uniformly across the wafer surface. Therefore, temperature uniformity across the wafer continues to be a critical issue even with the new annealing processes. Temperature nonuniformity may cause uneven activation of the implants, as well as excessive thermal stresses that can introduce crystallographic defects [3]. One major reason for the temperature nonuniformity arises from the difference in the absorptance of various device patterns in different regions of the wafer surface. Several studies have examined the radiative properties of different patterned structures on wafers and obtained reasonable agreement with experimental results. A quick review is given by Chen et al. [4].

Radiative properties of nano-structures may be very different from those of microstructures made of similar

* Corresponding author. Tel.: +1 321 674 7246; fax: +1 321 674 8813.
*E-mail address:* phsu@fit.edu (P.-f. Hsu).

0017-9310/$ - see front matter © 2008 Elsevier Ltd. All rights reserved.
doi:10.1016/j.ijheatmasstransfer.2008.03.003

**Nomenclature**

| | |
|---|---|
| $d$ | depth, m |
| $\mathbf{E}$ | electric field vector, V/m |
| $\mathbf{H}$ | magnetic field vector, C/m s |
| $i$ | square root of (−1); node index |
| $j$ | diffraction order; node index |
| $\mathbf{K}$ | grating vector, $m^{-1}$ |
| $\mathbf{k}$ | wavevector, $2\pi/\lambda$, $m^{-1}$ |
| $l$ | length, m |
| $n$ | refractive index; superscript for time step |
| $r_{pq}$ | Fresnel reflection coefficient from medium $p$ to $q$ |
| $t$ | transmission coefficient |
| $t_{pq}$ | Fresnel transmission coefficient from medium $p$ to $q$ |
| $\hat{\varepsilon}$ | electrical permittivity, $C^2/N\,m^2$ |
| $\hat{\mu}$ | magnetic permeability, $N\,s^2/C^2$ |
| $\hat{\sigma}$ | electrical conductivity, $C^2/N\,m^2\,s = (\Omega\,m)^{-1}$ |
| $\hat{\sigma}_M$ | magnetic conductivity, $N\,s/C^2$ |
| $\varepsilon_e$ | equivalent electrical permittivity, $C^2/N\,m^2$ |
| $\sigma_e$ | equivalent electrical conductivity, $C^2/N\,m^2\,s = (\Omega\,m)^{-1}$ |
| $\varepsilon$ | dielectric function |
| $\theta$ | polar angle, rad |
| $\kappa$ | extinction coefficient, $m^{-1}$ |
| $\lambda$ | wavelength in vacuum, m |
| $\phi$ | filling ratio |
| $\psi$ | amplitude of the magnetic field, C/m s |

*Greek symbols*

| | |
|---|---|
| $\alpha$ | absorptance |
| $\gamma$ | phase difference, rad |

materials [5]. It is essential to know the spectral-directional absorptance of the patterned wafers across a broad range of wavelengths, including the ultraviolet region, so the amount of energy absorbed from the flash-lamp can be determined accurately. The feature size of the new generation of semiconductor devices is already below 65 nm, which is smaller than the wavelength (200–1000 nm) of the flash-lamp annealing heat sources. Little is known about the influence of nanoscale patterns on the radiation absorption and reflection during the millisecond annealing process. The objective of the present research is to continue the prior work by Chen et al. [4] to model the radiative properties of periodically patterned wafers that include features expected in advanced CMOS device technologies. The effects of wafer temperature, wavelength, polarization, and angle of incidence on the spectral directional-hemispherical directional absorptance are investigated for selected two-dimensional (2D) patterned structures with multilayer gratings. In the present study, the rigorous couple wave analysis (RCWA) [6–9] and finite-difference time-domain (FDTD) methods are employed to numerically solve the Maxwell equations and obtain the radiative properties of various wafer front side geometries. For periodic structures, RCWA can produce accurate solutions much faster than FDTD. The FDTD method incorporates a Debye time-domain optical property model for treating the Si optical constants at the wavelengths where the extinction coefficient ($\kappa$) is greater than the refractive index ($n$) [10].

Previous studies have used the method of homogenization or effective medium theory (EMT), in which the grating region is treated as a homogeneous layer with an effective dielectric function. This way, the 2D patterned structures are simplified to planar multilayer structures, which allows the use of very fast calculations based on the matrix equations of thin film optics [11,12]. The EMT is often helpful for understanding the behavior of subwavelength gratings with small period-to-wavelength ratios. By using RCWA in the small-depth limit, it has been shown that the effective properties of subwavelength gratings strongly depend on the grating depth [13]. Moreover, the effective properties have been shown to depend not only on the grating structure but also on the optical indices of the surrounding media. A simple expression for the effective indices of 1D and 2D gratings with arbitrary depths was proposed. Comparison with rigorous computations showed that for transverse electric polarization of 1D gratings the depth dependence of the effective index prediction is accurate [13].

In this study, the structures considered include Si gratings and $SiO_2$ trenches embedded in the Si substrate. The wavelength range of the radiation from the heat source covers from 200 to 1000 nm. The incident radiation is at normal or arbitrary angles of incidence with the plane of incidence perpendicular to the gratings or trench lines. Earlier investigations explored the behavior for relatively simple patterns with features on the order of micrometers and at wavelengths longer than 400 nm, i.e., ultraviolet wavelengths were not considered [14–17]. This study expanded the prior work by the authors. Furthermore, extensive feature size variations, in conjunction with the wavelength variations, were considered for three different nano-structures on the wafer front side. The effects of the resonant cavity, diffraction, wave interferences on the spectral-directional absorptance were discussed.

## 2. Theoretical analysis

Two rigorous methods were used in this work: FDTD and RCWA. A much simpler and physically intuitive EMT was also used to help explain the absorptance pre-

dicted by the two methods. The purpose was to understand the pattern and the device size scaling on the resulting spectral-directional absorptance. Three different groups are used and the geometries are illustrated in Fig. 1 for patterned structures for CMOS devices. In Fig. 1a, a periodic pattern is formed on a Si wafer that includes trenches filled with $SiO_2$, which provide electrical insulation between active areas of the device where transistors are formed. Fig. 1b depicts a polysilicon gate array on the Si substrate, while Fig. 1c gives important parameters needed in the analysis of the absorptance of the patterned wafer, upon which the electromagnetic wave irradiates. A plane wave is incident on a 1D grating surface from free space by neglecting the effect of gases in the RTP chamber. Region I is free space with $\varepsilon_I = n_I = 1$ and $\kappa_I = 0$, where $\varepsilon = (n + i\kappa)^2$ is the dielectric function. Region II is composed of materials A and B such that its dielectric function is a periodic function of $x$ with a period $\Lambda$, which is the grating period. The filling ratio of material A is $\phi$, and the lateral extension of the gratings is assumed to be infinite. Region III is the substrate with a dielectric function, $\varepsilon_{III}$. The wavevector **k** defines the direction of incidence, and the angle between **k** and the surface normal ($z$-axis) is the angle of incidence $\theta$, also called the polar angle. The grating vector **K** for the structure shown in the figure is defined in the positive $x$ direction with a magnitude $K = 2\pi/l_p$. For simplicity, it is assumed that incidence wavevector is on the $x$–$z$ plane, that is, the $y$ component of **k** is zero. For a transverse magnetic (TM) wave, the magnetic field **H** is perpendicular to the plane of incidence, i.e., parallel to the $y$ direction and perpendicular to the grating vector **K**, as shown in Fig. 1c. On the other hand, for a transverse electric (TE) wave, the electric field **E** is perpendicular to the plane of incidence and the vector **K**. The following discussion is for the TE wave. The magnitude of the incident electric field, after normalization, can be expressed as $\exp(ik_x x + ik_z z - i\omega t)$, where $k_x$ and $k_z$ are respectively the $x$ and $z$ components of **k** (the wave vector), $\omega$ is the angular frequency, and $t$ is time. For simplicity, the time harmonic term $\exp(-i\omega t)$ will be omitted hereafter. The dimensions of the structures examined in this study are listed in Table 1. Although real device structures comprise

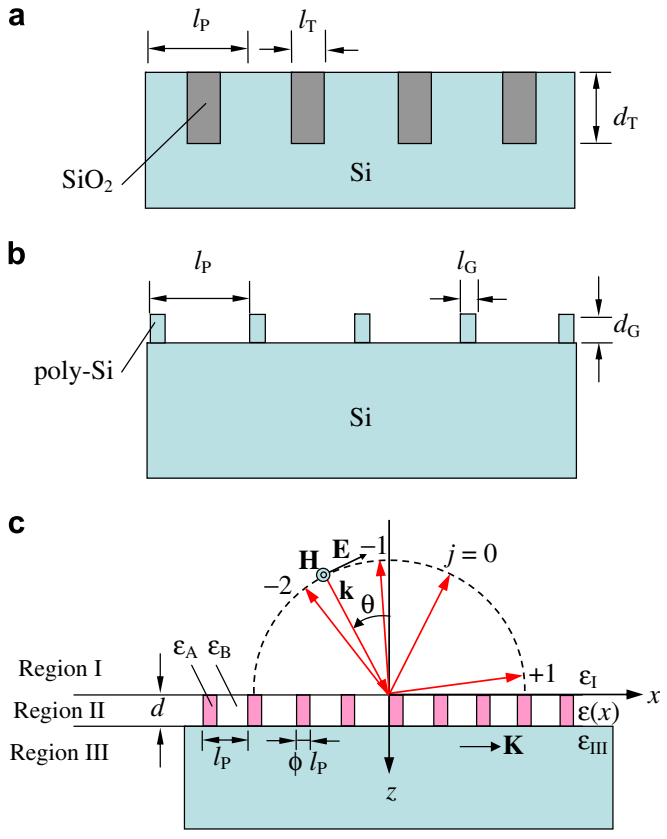


Fig. 1. Illustrations of the device and model structures. (a) Parameters for cases A3 and A4; (b) parameters for case B1; (c) geometry of the problem (TM mode).

Table 1
Geometry of studied structures

| A3 | $l_T$ | $l_P$ | $l_T/l_P$ |
|---|---|---|---|
| 1 | 20 | 40 | 0.50 |
| 2 | 20 | 80 | 0.25 |
| 3 | 20 | 200 | 0.10 |
| 4 | 20 | 400 | 0.05 |
| 5 | 50 | 100 | 0.50 |
| 6 | 50 | 200 | 0.25 |
| 7 | 50 | 500 | 0.10 |
| 8 | 50 | 1000 | 0.05 |
| 9 | 100 | 200 | 0.50 |
| 10 | 100 | 400 | 0.25 |
| 11 | 100 | 1000 | 0.10 |
| 12 | 100 | 2000 | 0.05 |
| **A4** | $l_T$ | $l_P$ | $l_T/l_P$ |
| 1 | 10 | 50 | 0.2 |
| 2 | 20 | 100 | 0.2 |
| 3 | 40 | 200 | 0.2 |
| 4 | 80 | 400 | 0.2 |
| 5 | 40 | 80 | 0.5 |
| 6 | 80 | 160 | 0.5 |
| 7 | 160 | 320 | 0.5 |
| 8 | 320 | 640 | 0.5 |
| 9 | 160 | 200 | 0.8 |
| 10 | 320 | 400 | 0.8 |
| 11 | 640 | 800 | 0.8 |
| 12 | 1280 | 1600 | 0.8 |
| **B1** | $l_G$ | $l_P$ | $l_G/l_P$ |
| 1 | 30 | 60 | 0.50 |
| 2 | 30 | 120 | 0.25 |
| 3 | 30 | 300 | 0.10 |
| 4 | 30 | 600 | 0.05 |
| 5 | 20 | 40 | 0.50 |
| 6 | 20 | 80 | 0.25 |
| 7 | 20 | 200 | 0.10 |
| 8 | 20 | 400 | 0.05 |
| 9 | 10 | 20 | 0.50 |
| 10 | 10 | 40 | 0.25 |
| 11 | 10 | 100 | 0.10 |
| 12 | 10 | 200 | 0.05 |

Device dimensions are in the unit of nm; trench depth $d_T$ and gate height $d_G$ are constant at 300 nm and 100 nm, respectively.

a mixture of isolation areas and active areas containing gates, in this study we attempt to uncover the basic phenomena introduced by each type of feature by studying the effects of arrays of trenches and arrays of silicon gates separately. In reality, the gates are isolated from the Si substrate by a very thin dielectric film. Because this dielectric film is only about 1 nm thick, it is neglected in the model. The gates are usually made of polysilicon, but in this study they have been modeled as being made of silicon. Because poly-Si occupies a small volume fraction only, the use of the optical constants of silicon should not cause significant errors. This study assumes that the structures are 1D gratings and the depth of the gates is fixed at $d_G = 100$ nm while the depth of the trenches is fixed at $d_T = 300$ nm. The effects of period $l_P$, width of the trench $l_T$, and the width of the gate $l_G$ on the absorptance are explored.

The three groups of structures explored help us understand the consequences of variations in the density of patterns on wafers, as reflected in the ratio of the pattern pitch to the width of isolation regions (oxide trenches), active regions (silicon) or gate width. They also allow us to see what happens as dimensions are reduced for further device scaling.

Group A3: This group helps us explore the effect of varying the ratio of isolation width (oxide trenches) to the pattern pitch, for three sets of fixed trench widths. For each set the ratio of isolation width to pitch varies from 5% up to 50%, while the three sets explore trench width scaling from 100 nm down to 20 nm.

Group A4: This group helps us explore the effect of varying the active area (silicon) width, for three sets of fixed isolation density (the ratio of the trench width to the pitch). The three sets cover isolation densities of 20%, 50% and 80%. In each set the active area width takes values of 40, 80, 160 or 320 nm. The isolation trench width and the pattern pitch are set to be consistent with the isolation density and active area size.

Group B1: This group helps us explore the effect of varying the ratio of gate width (silicon bars) to the pattern pitch, for three sets of fixed gate widths. For each set the ratio of gate width to pitch varies from 5% up to 50%, while the three sets explore gate width scaling from 30 nm down to a very narrow gate width of 10 nm.

### 2.1. Finite-difference time-domain method

The direct numerical simulation of electromagnetic wave propagation can be carried out with the finite-difference time-domain solution method of the Maxwell equations. The rigorous solution allows one to understand the wave propagation process and compare the experimental measurements after making a few assumptions, which are typical in analytical models. Maxwell's equations take the following form for a linear isotropic material (the two Gaussian laws are not used in the FDTD solution):

$$\hat{\varepsilon}\frac{\partial \mathbf{E}}{\partial t} = \nabla \times \mathbf{H} - \hat{\sigma}\mathbf{E} - \mathbf{J}_s \tag{1}$$

$$\hat{\mu}\frac{\partial \mathbf{H}}{\partial t} = -\nabla \times \mathbf{E} - \hat{\sigma}_M\mathbf{H} - \mathbf{M}_s \tag{2}$$

$\mathbf{J}_s$ and $\mathbf{M}_s$ are the electrical and magnetic field sources; $\hat{\varepsilon}$, $\hat{\mu}$, $\hat{\sigma}$, and $\hat{\sigma}_M$ are the permittivity, permeability, electrical conductivity, and magnetic conductivity or equivalent magnetic loss of the material, respectively. Note that $\hat{\varepsilon} = \varepsilon_0\varepsilon$, where $\varepsilon_0$ is the permittivity value in vacuum. In the current problem, $\mathbf{J}_s$ and $\mathbf{M}_s$ are zero. In this study, the 1D grating structures have to be solved in the 2D space. Maxwell's equations are split into two sets for two polarizations: the TE polarization and the TM polarization. Furthermore, since the material properties are complex numbers, to adapt them to real number computation, their equivalent real properties $\varepsilon_e$, $\sigma_e$ are used ($\hat{\mu} = \mu_0$, $\hat{\sigma}_M = 0$ in the current problem) [10]. By replacing the electric and magnetic fields with their vector components and employing the equivalent properties [10], the 2D TE set of equations is

$$\varepsilon_e\frac{\partial E_y}{\partial t} = \frac{\partial H_z}{\partial x} - \frac{\partial H_x}{\partial z} - \sigma_e E_y \tag{3a}$$

$$\mu\frac{\partial H_x}{\partial t} = -\frac{\partial E_y}{\partial z} - \sigma_M H_x \tag{3b}$$

$$\mu\frac{\partial H_z}{\partial t} = \frac{\partial E_y}{\partial x} - \sigma_M H_z \tag{3c}$$

The 2D TM set of equations is similarly obtained for $H_y$, $E_x$, and $E_z$, which are field vector components in the coordinate directions shown in Fig. 1c. In fact, TM set is the dual form of the TE set, i.e., the two sets of equations are mathematically equivalent. Therefore, a solution to either set of equation will take the same mathematical form. The above equations are coupled linear first-order partial differential equations.

The detailed numerical scheme, periodic boundary treatment, and perfectly matched layer absorbing boundary condition can be found in many references, including Taflove and Hagness [18] and our previous work [19]. Only the essential difference equations are presented below. For a 2D geometry, the solutions for the TE wave with a second-order central-difference scheme can be written as

$$E_y^n(i,j) = \frac{\varepsilon_e - \sigma_e\Delta t/2}{\varepsilon_e + \sigma_e\Delta t/2}E_y^{n-1}(i,j) + \frac{\Delta t}{\varepsilon_e + \sigma_e\Delta t/2} \times \left\{\frac{1}{\Delta x}\left[H_z^{n-1/2}(i+1/2,j) - H_z^{n-1/2}(i-1/2,j)\right] - \frac{1}{\Delta z}\left[H_x^{n-1/2}(i,j+1/2) - H_x^{n-1/2}(i,j-1/2)\right]\right\} \tag{4a}$$

$$H_x^{n+1/2}(i,j+1/2) = \frac{\mu-\sigma_M\Delta t/2}{\mu+\sigma_M\Delta t/2}H_x^{n-1/2}(i,j+1/2) - \frac{\Delta t}{(\mu+\sigma_M\Delta t/2)\Delta z}\left[E_y^n(i,j+1)-E_y^n(i,j)\right] \quad (4b)$$

$$H_z^{n+1/2}(i+1/2,j) = \frac{\mu-\sigma_M\Delta t/2}{\mu+\sigma_M\Delta t/2}H_z^{n-1/2}(i+1/2,j) + \frac{\Delta t}{(\mu+\sigma_M\Delta t/2)\Delta x}\left[E_y^n(i+1,j)-E_y^n(i,j)\right] \quad (4c)$$

where the superscript of the field components stands for time step index ($n$) and the subscript represents the vector component: $x$ is the grating groove direction, $z$ is the height direction, $y$ is normal to the paper plane. $\Delta t$ is the time step size used in the time derivative terms. Note that in Eq. (4), $\sigma_e$ and $\sigma_M$ are set to zero for ideal dielectric and non-magnetic materials. According to Yee's notation, a spatial point in a Cartesian coordinate that is written as ($i$, $j$) corresponds to the co-ordinates ($i\Delta x$, $j\Delta z$), where, $\Delta x$ and $\Delta z$ are the lattice space increments in the $x$ and $z$ directions, and $i$ and $j$ are integer indices. The calculations were carried out on a 48-processor Beowulf cluster, and the mesh size used was 5 nm. Smaller mesh sizes were used to verify the accuracy of larger mesh size – it is found that there is little difference between the 2 nm and 5 nm mesh solutions. The time step ($\Delta t$) size is based on the Courant–Friedrichs–Lewy criterion [19] and is on the order of $10^{-16}$ s.

### 2.2. Rigorous coupled-wave analysis

Since the RCWA formulation was presented only for the TE wave incidence in previous work [4], RCWA for the TM wave incidence is briefly illustrated here. Note that the plane of incidence is perpendicular to the grating grooves, such that all the diffracted waves lie in the same plane as the plane of incidence. The normalized magnetic field in region I shown in Fig. 1c is a superposition of incidence field and all reflected wave field and is expressed as

$$H_I(x,z) = \exp(ik_x x + ik_z z) + \sum_j H_{rj}\exp(ik_{xj}x - ik_{zj}^r z) \quad (5)$$

where $k_x$ and $k_z$ are the $x$- and $z$-components of $\mathbf{k}$, and $H_{rj}$ is the amplitude of the $j$th order reflected wave magnetic field normalized to the incidence. The subscript or superscript "$r$" symbols the reflected wave. The magnitude of $\mathbf{k}$ in regions I and III can be expressed as

$$k_I = \frac{2\pi n_I}{\lambda} = \frac{2\pi}{\lambda} = k \quad \text{and} \quad k_{III} = \frac{2\pi}{\lambda}\sqrt{\varepsilon_{III}} = k\sqrt{\varepsilon_{III}} \quad (6)$$

where $n_I$ is the refractive index in region I. It should be mentioned that $\varepsilon$ here denotes dielectric function which is a complex number whose value equals $(\varepsilon_e + i\sigma_e/\omega)/\varepsilon_0$. $k_{xj}$ is determined by the Bloch–Floquet condition [4]:

$$k_{xj} = \frac{2\pi}{\lambda}\sin\theta + \frac{2\pi}{l_P}j = k_x + Kj \quad (7a)$$

The above equation can be expressed in terms of the zenith angle of reflection:

$$\sin\theta_j = \sin\theta + \frac{j\lambda}{l_P} \quad (7b)$$

where $\theta_j = \sin^{-1}(k_{xj}/k)$ is the $j$th order diffraction angle for reflection and Eq. (7b) is the well-known grating equation. The $z$ component of $\mathbf{k}$ for the $j$th order reflected wave is

$$k_{zj} = \begin{cases} \left(k^2 - k_{xj}^2\right)^{1/2}, & k > k_{xj} \\ i\left(k_{xj}^2 - k^2\right)^{1/2}, & k_{xj} > k \end{cases} \quad (7c)$$

Note that the incidence magnetic field magnitude is assumed to be unity such that $H_{rj}$ equals to $r_j$, which is the Fresnel reflection coefficient. The normalized magnetic field in region III with respect to the incidence is expressed as

$$H_{III}(x,z) = \sum_j H_{tj}\exp(ik_{xj}x + ik_{zj}^t z) \quad (8)$$

where $H_{tj}$ is the amplitude of the $j$th order transmitted wave. Similarly, the subscript or superscript "$t$" symbols the transmitted wave. The normalized magnetic field in region II with respect to the incidence is

$$H_{II}(x,z) = \sum_j \psi_{yj}(z)\exp(ik_{xj}x) \quad (9)$$

where $\psi_{yj}(z)$ the amplitude for the $j$th space-harmonic of magnetic field in the grating region. From the Maxwell equations, the magnetic field, which lies only in the $y$ direction, can be expressed in the form of the related electric field:

$$H_{II} = H_{II,y} = \frac{i}{\omega\mu_0}\left(\frac{\partial E_{II,z}}{\partial x} - \frac{\partial E_{II,x}}{\partial z}\right) \quad (10)$$

where the two partial derivatives of electric field components can also be expressed by the magnetic field, such that the magnetic field in region II should satisfy equations below:

$$\frac{\partial}{\partial z}\left(\frac{\partial H_{II,y}}{\partial z}\right) = -\varepsilon(x)\left\{\frac{\partial}{\partial x}\left[\frac{1}{\varepsilon(x)}\left(\frac{\partial H_{II,y}}{\partial x}\right)\right] + k^2 H_{II,y}\right\} \quad (11)$$

where the left side of Eq. (11) is a continuous function while $\varepsilon(x)$ has jump discontinuities at the interface between material A and B. As a result, the right hand side must be the product of two functions, which only have pairwise-complementary jump discontinuities. For such product of two functions, its Fourier coefficients can be expressed by those of the inverse of one function and those of the ordinary of the other function based on the inverse rule [8]. These Fourier coefficients are important for RCWA obtaining radiative properties later. Here, the inverse of the function $\varepsilon(x)$, which is $1/\varepsilon(x)$, is expanded as a Fourier series below:

$$\frac{1}{\varepsilon(x)} = \sum_m \varepsilon_m^{\text{inv}} \exp\left(\mathrm{i}\frac{2m\pi}{l_P}x\right) \tag{12}$$

where $\varepsilon_m^{\text{inv}}$ is the $m$th Fourier coefficient for $1/\varepsilon(x)$ and not a physical property for passive medium. On the other hand, the Fourier series of $\varepsilon(x)$ is expressed as

$$\varepsilon(x) = \sum_m \varepsilon_m^{\text{ord}} \exp\left(\mathrm{i}\frac{2m\pi}{l_P}x\right) \tag{13}$$

where $\varepsilon_m^{\text{ord}}$ is the $m$th Fourier coefficient of $\varepsilon(x)$ and not a physical property for passive medium as well. Caution must be taken because $\varepsilon_m^{\text{inv}} \neq 1/\varepsilon_m^{\text{ord}}$ for most cases. In order to solve Eq. (11), one should also be careful when handing the Fourier series of the terms in the brace at the right side of the equation. Failure of correctly Fourier factorizing functions can result in slow convergence and even erroneous solutions [8]. Consequently, Eq. (11) can be rearranged in terms of $j$th order in $\exp(\mathrm{i}k_{xj}x)$ as follows:

$$\sum_j \left(\sum_m \varepsilon_{j-m}^{\text{inv}} \frac{\partial^2 \psi_{ym}}{\partial z^2} - \sum_m k_{xj} \left\|\varepsilon^{\text{ord}}\right\|_{j,m}^{-1} k_{xm}\psi_{ym} + k^2\psi_{yj}\right) \times \exp(\mathrm{i}k_{xj}x) = 0 \tag{14}$$

where $\|\varepsilon^{\text{ord}}\|^{-1}$ is the inverse of matrix $\mathbf{M}$, (i.e., $\mathbf{M}^{-1}$). $\mathbf{M}$ is the Toeplitz matrices [8] generated by the Fourier coefficients of the dielectric function such that the element of matrix $\mathbf{M}$ is $M_{l,p} = \varepsilon_m^{\text{ord}}$, where $m = l - p$, $l$ and $p$ are positive integers. A sufficiently large number of diffraction orders must be included for the calculation to be accurate although most diffraction order far-field efficiency is zero. Eq. (14) can be represented in a matrix form and solved by obtaining its eigenvalue. Boundary conditions require that the tangential components of the electric and magnetic fields be continuous at the boundaries between different regions. The field components are consistent for all $x$ once the boundary conditions are satisfied at $x = 0$ because of the Bloch–Floquet condition. After substituting the boundary conditions, the electromagnetic fields in different regions can be solved. Consequently, the diffraction efficiencies and radiative properties of periodic structures can be obtained.

### 2.3. Effective medium theory

Apart from FDTD and RCWA, other simplified modeling algorithms may provide fast calculation speed with reasonable accuracy. Some previous studies have used the method of homogenization, and the underlying physics is based on the EMT [6,7,11,12,20]. The EMT may be valid when the grating period is much shorter than the wavelength because all the diffracted waves are evanescent waves, except the zeroth-order in specular direction. As a result, the radiative properties of periodic structures can be treated as those of a homogeneous layer with an effective dielectric function. This way, the patterned structures are simplified to planar multilayer structures, which requires much less computation time to solve the matrix equations based on thin film optics.

Although the effective dielectric function has been proposed in different ways and includes multiple terms, adding more terms (orders) does not always guarantee better approximation [4]. Moreover, the simplest (zeroth-order) expressions have been successfully used for anti-reflection coating design [12]. As a result, the zeroth-order expressions first proposed by Rytov [21] are employed here. The zeroth-order effective dielectric function for a mixture of materials A and B is given below:

$$\hat{\varepsilon}_{\text{TE}} = \phi\hat{\varepsilon}_{\text{A}} + (1-\phi)\hat{\varepsilon}_{\text{B}} \quad \text{and}$$
$$\hat{\varepsilon}_{\text{TM}} = \left(\frac{\phi}{\hat{\varepsilon}_{\text{A}}} + \frac{1-\phi}{\hat{\varepsilon}_{\text{B}}}\right)^{-1} \tag{15}$$

where $\phi$ is the filling ratio of material A and subscripts TE and TM indicate the polarization of the incident light. For modeling structures in the present work, the grating region will be homogenized into a film with the same thickness but different effective dielectric function based on the EMT.

## 3. Results and discussion

Comparison of the results obtained by the FDTD and RCWA methods reveals good agreement between these two sets of solutions. The agreement verified the validity of the use of FDTD and RCWA to study grating effects that lead to rather complicated absorptance (or reflectance) curves for different conditions. To analyze how the absorptance curves are affected by device size, i.e., device scaling, the following factors are included: grating geometries and structure, wavelength, polarization, angle of incidence, and the wavelength- and temperature-dependent optical constants.

First, we consider normal incidence and a temperature of 910 °C. The optical constants of silicon and $SiO_2$ are shown in Fig. 2 [4]. The optical constants of $SiO_2$ are assumed to be independent of temperature.

The absorptance of bare Si, $SiO_2$ and $SiO_2$-over-Si (300 nm $SiO_2$ film thickness) are shown in Fig. 3. The $SiO_2$ has the lowest $n$ value which thus allows more incident energy to penetrate and thus has the highest transmittance. The absorptance of $SiO_2$-over-Si depicts the typical oscillations that arise in thin film coatings [22].

### 3.1. Trench structures in the A3 and A4 groups

Fig. 4 shows the absorptance from structure A3 with different geometric sizes. The A3 group cases have four different filling ratios. For each filling ratio, the trench width ($l_T$) increases from 20, 50, to 100 nm. Thus, this group has a total of 12 geometry sizes (Table 1). Fig. 4a shows clear interference effects at long wavelengths. For the TE wave, the interference appears at wavelength longer than 540 nm. According to thin film theory, interference happens when the extinction coefficient is small enough, or

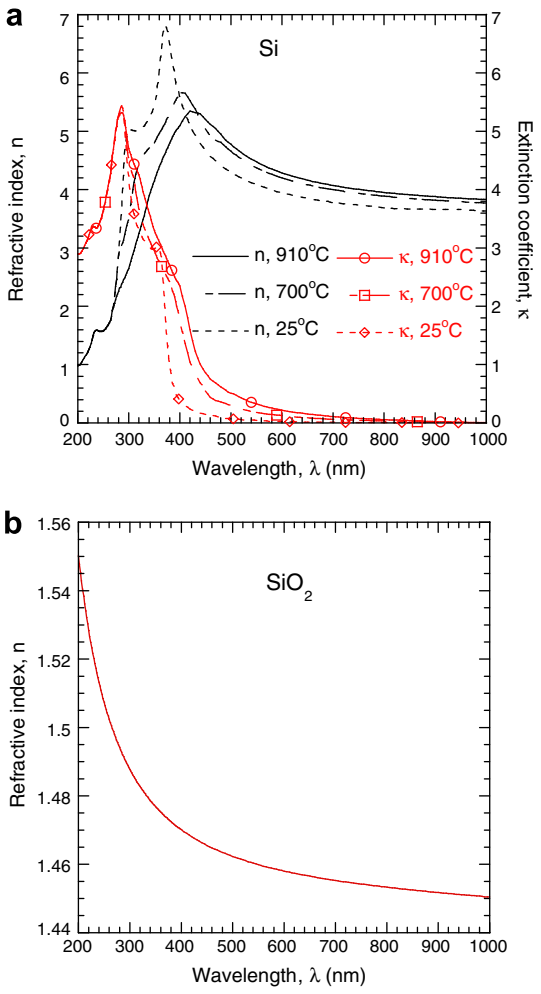


Fig. 2. Optical constants of the materials (data based on Ref. [4]). (a) Refractive index and extinction coefficient of Si; (b) refractive index of $SiO_2$.

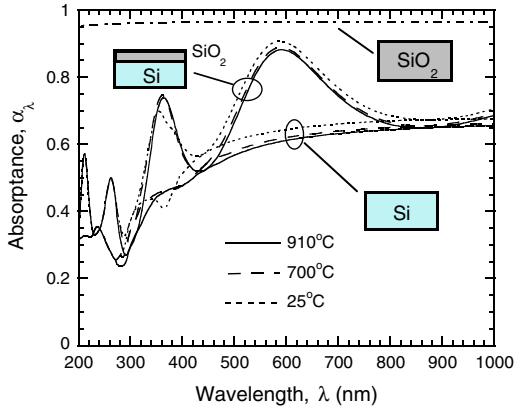


Fig. 3. Absorptance spectra of Si, $SiO_2$, and $SiO_2$-over-Si at different temperatures.

$\kappa d_T/\lambda$ is small enough, which is verified in Fig. 2. Note that the multiple reflection effect starts at a much shorter wavelength for the TM wave. If we use the concept of effective medium theory and consider the mixture of $SiO_2$ and Si as a homogeneous, effective medium, then this becomes a thin film problem. Since the effective medium is not isotropic, the dielectric function can be written as $\hat{\varepsilon}_{TE}$ and $\hat{\varepsilon}_{TM}$. The $SiO_2$ is insulating, which makes the overall conductivity along grating direction smaller than the average of Si and $SiO_2$, so the extinction coefficient $\kappa$ becomes smaller than the average. In thin film theory, the smaller the $\kappa$ is, the stronger the interference effect will become. This explains why multiple reflection effect starts at a shorter wavelength in the TM wave as in the case A3-1.

Fig. 4 also shows the EMT prediction improves when the $l_T/l_P$ ratio is small except at short wavelength. It is of course true when the ratio is close to 1. This is because the TE and TM absorptance curves approach to those of pure Si or $SiO_2$ when the $l_T/l_P$ ratio decreases to zero or increases to 1. However, EMT does not agree with FDTD at short wavelengths for the TM wave, as shown in Fig. 4a, and the absorptance of TM wave from EMT in Fig. 4d clearly shows oscillations that are not predicted by the FDTD method. The reason is that EMT simplifies the grating structure into a uniform medium with effective dielectric constants, which requires the grating's geometrical size to be smaller than the wavelength. For the short wavelengths in Fig. 4a, the EM wave could be treated as ray tracing energy bundles which separates the reflection from Si and that from $SiO_2$ trench, instead of the diffractive wave which is not significant at short wavelengths and does not distinguish the reflected waves from either region. This can affect the penetration depth. Fig. 5a shows the effective extinction coefficient $\kappa$ from EMT, with $l_T/l_P = 0.5$. The incident TM wave in nearly all wavelengths considered can easily penetrate the trench depth of 300 nm. That is why there is strong interference effect at short wavelengths in the EMT result. However, the actual penetration depth of Si at 910 °C is much smaller, as shown in Fig. 5b. At wavelengths smaller than 630 nm, the incident wave cannot penetrate 300 nm in Si, thus a weaker interference at short wavelengths in the FDTD TM polarization results in Fig. 4a. Another reason is that the zeroth-order EMT dielectric function, Eq. (15), can not account for the optical constants effect from the homogeneous layers above and below the device or grating layer, as explained in [13]. It should be recognized that in general the EMT TM wave prediction is less accurate than that by EMT TE wave.

When the grating period is significantly larger than wavelength, the small Si substrate between trenches only affects the neighboring region, not the whole period. That means the thin film effect will be much weaker than what is predicted by EMT. Two pairs (A3-5 and A3-6) of absorptance curves with the same $l_T/l_P$ ratios, as those in Fig. 4a and b but $l_T = 50$ nm, are presented in Fig. 6. Comparing Figs. 4 and 6, the EMT results in Fig. 4 are more accurate than that in Fig. 6. This conclusion can be further verified in Fig. 7, in which $l_T/l_P$ is maintained at 0.2 but $l_P$ varies from 50 to 400 nm. In Fig. 7a, the EMT result agrees well with FDTD result (only FDTD is plotted). With the increase of period, the agreement becomes worse (note that

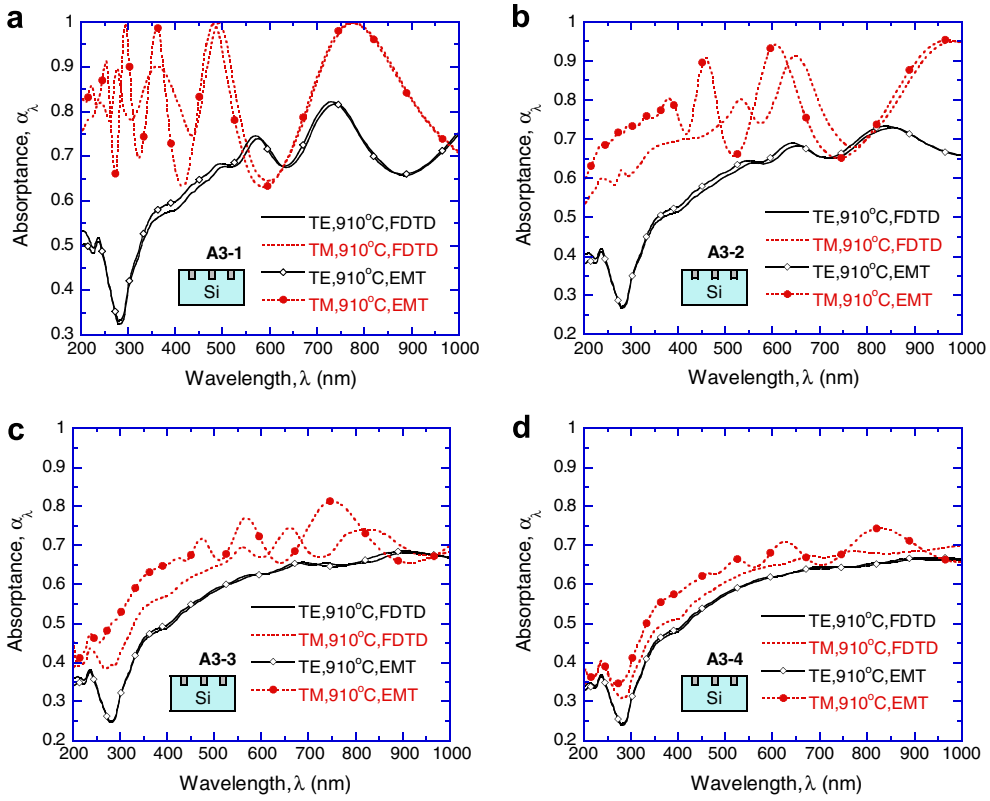


Fig. 4. Absorptance spectra for A3 cases at $\theta = 0°$, $l_T = 20$ nm. (a) $l_P = 40$ nm, $l_T/l_P = 0.5$; (b) $l_P = 80$ nm, $l_T/l_P = 0.25$; (c) $l_P = 200$ nm, $l_T/l_P = 0.1$; (d) $l_P = 400$ nm, $l_T/l_P = 0.05$.

the EMT result does not change according to Eq. (15)), and TE and TM results are closer to each other. It is noted that when EMT gives a good prediction in Fig. 7a of Case A4-1, the period size (50 nm) is far smaller than the shortest wavelength (200 nm) of the light source. As the period sizes gradually increases to 400 nm in Case A4-4 (Fig. 7d, $l_P = 400$ nm), the EMT prediction was not good.

The high TM wave absorptance at some wavelengths of the trench structures, e.g., the absorptance $\alpha_\lambda$ reaches 1 at 800 nm of Case A3-5 in Fig. 6a, needs careful examination. Fig. 8 shows the TM mode Poynting vector magnitude distribution of Case A3-5 at 800 nm wavelength. In Fig. 8, PML stands for the perfectly matched layer, which is an absorbing boundary condition. The Poynting vector plot clearly indicates the incident wave easily penetrates into the trench $SiO_2$ and little energy is able to go through the neighboring Si regions in layer II (Fig. 1c). The trench acts like an open valve or a wave guide.

Fig. 6 results indicate that the absorptance curves of different dimensions are similar to those in Fig. 4 with the same $l_T/l_P$ but with a slight spectral shift, except at short wavelengths where the TE wave absorptance has a drastic increase, i.e., at $\lambda = 200$ nm. The absorptance increase can also be found in Fig. 7c. By comparing different geometry sizes in Figs. 6 and 7, it is found that the absorptance increase appears only in the TE polarized wave, and is highly dependent on trench width – that is, the increase will shift towards longer wavelength with the increase of trench width. According to Fresnel equations, the reflectance at oblique incident angle from vacuum to Si for the TE mode is higher than that for the TM mode, and considering the relation between trench size and the absorptance peak position, it can be concluded that the absorptance increase is caused by trench resonance "cavity" effect [23].

Fig. 9 shows absorptance of trench structures with a large filling ratio (0.8) and larger periods (200–1600 nm), e.g., in Fig. 9a, at short wavelengths ($\lambda < 300$ nm) the absorptance curves have strong oscillations. Due to the large extinction coefficient of Si at short wavelengths, the oscillation cannot be caused by thin film interference. Therefore, the interference is generated from the coherent interactions of the reflection on trench cavity and the direct reflection on the Si between trenches. When comparing Figs. 4, 6, 7 and 9, we find that these phenomena only appear when the period or pitch is comparable to the wavelength and $l_T/l_P$ is not too small. When the period is much smaller than the wavelength, the wavelength will be bigger than the microcavity cutoff wavelength (see discussion in the Section 2). Thus, there is no resonance cavity effect. On the other hand, while the period is much larger than wavelength (as in Fig. 9c and d), the reflections from Si and $SiO_2$ are considered separately and the absorptance will be the filling ratio weighted average of two separate reflectances. The effect of $l_T/l_P$ is also evident, because the interference is strong only if the amplitudes of the reflected wave from the $SiO_2$ trench and that from Si substrate are

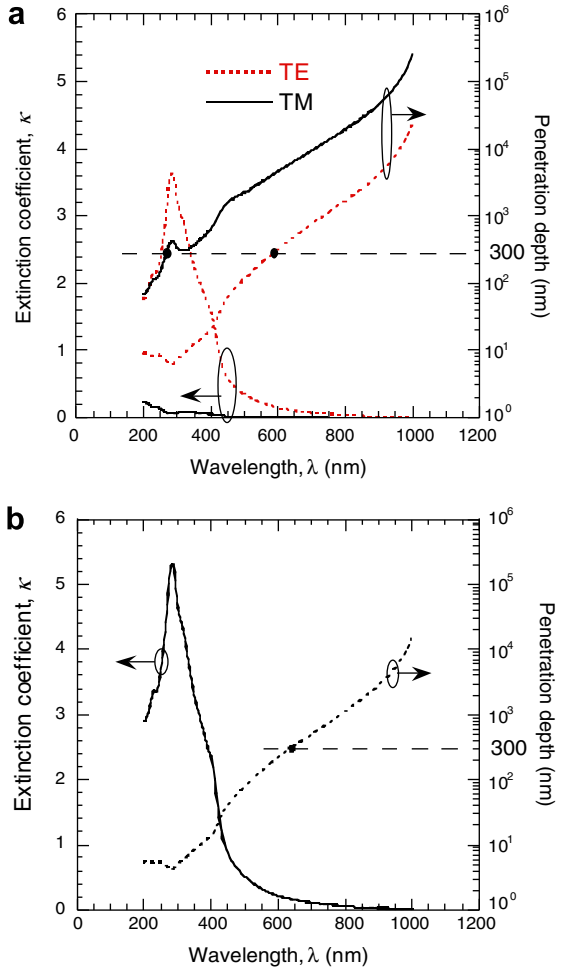


Fig. 5. Extinction coefficient and penetration depth of A3(a) case. (a) Penetration depths based on EMT effective extinction coefficients in two polarizations; (b) actual penetration depth based on the extinction coefficient of Si.

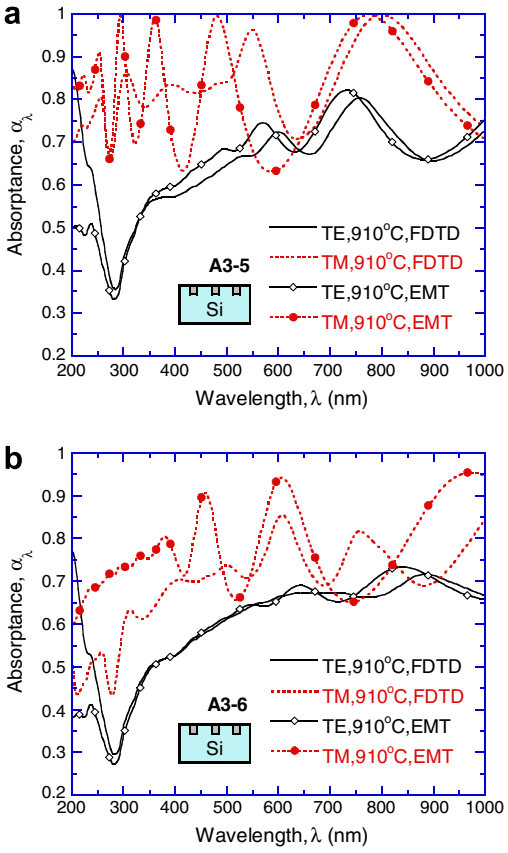


Fig. 6. Absorptance spectra for A3-5 and A3-6 cases at $\theta = 0°$, $l_T = 50$ nm. (a) $l_P = 100$ nm, $l_T/l_P = 0.5$; (b) $l_P = 200$ nm, $l_T/l_P = 0.25$.

about the same, which would not happen if $l_T/l_P$ is too small. Comparing the cases A3-1 (Fig. 4a, $l_P = 40$ nm, $l_T/l_P = 0.5$) and A3-5 (Fig. 6a, $l_P = 100$ nm, $l_T/l_P = 0.5$), it is clear that the EMT results are more accurate when the period is small compared to the wavelength, i.e., subwavelength gratings.

Fig. 9 depicts the influence of temperature on the absorptance. The temperature effect could have been on the amplitude and phase shift, but overall it doesn't change absorptance curve much. This does, however, simplify the radiant energy absorption/reflection analysis on the the Si wafer front side when its temperature changes.

The A4 cases are considered to examine the effect of varying the period at the constant $l_T/l_P$ ratio. From the results of A4-1 to A4-4, it is found that the absorptance spectra for different period sizes are all similar to that for plain Si. The only obvious difference is at the short wavelength part of A4-4 TE absorptance, where strong interference effects are observed. This, as discussed before, may be caused by the coherent interactions between the reflection from $SiO_2$ trench and that from the neighboring Si substrate. This effect becomes stronger in A4-6, A4-7, and A4-8 cases where $l_T/l_P$ ratio increases to 0.5 and the periods are also larger compared to the A4-1 to A4-4 cases. A4-4 and A4-6 cases both have the same $l_T$, but A4-4 has the smaller filling ratio ($l_T/l_P$) and larger $l_P$. In the cases A4-9 to A4-12 with filling ratio = 0.8 and much larger period, the absorptance curves are more like that of an unpatterned 300 nm thick $SiO_2$ film on plain silicon. The A4-4 and A4-10 cases have the same $l_P$ but different $l_T$. Case A4-10 approaches that of the thin film interference pattern as its filling ratio is much larger. In addition, although A4-4, A4-8, and A4-12 all have the same space distance (320 nm) between trenches, but their absorptances are quite different – from close to pure Si absorption (A4-4) to close to thin film absorption (A4-12). As has been shown so far, the filling ratio and the period have stronger influence on the absorptance than the trench size.

### 3.2. Gate structures in the B1 group

The absorptance by B1 structures is shown in Fig. 10. While the gate sizes, ranging from 10 nm to 30 nm, are very small compared to wavelength, the numerical results show rather unusual phenomena. The FDTD and RCWA absorptance results of B1 cases are in good agreement. Therefore, only the FDTD result is presented. Fig. 10a

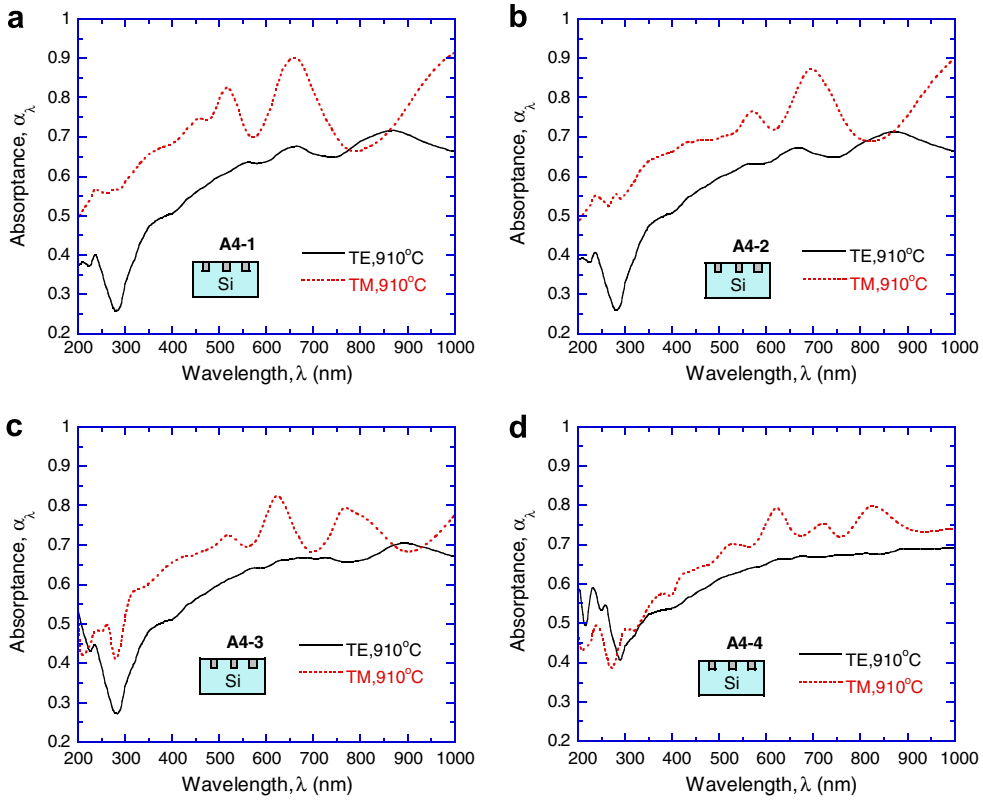


Fig. 7. Absorptance predicted by FDTD for A4 cases at $\theta = 0°$, $l_T/l_P = 0.2$. (a) $l_T = 10$ nm, $l_P = 50$ nm; (b) $l_T = 20$ nm, $l_P = 100$ nm; (c) $l_T = 40$ nm, $l_P = 200$ nm; (d) $l_T = 80$ nm, $l_P = 400$ nm.

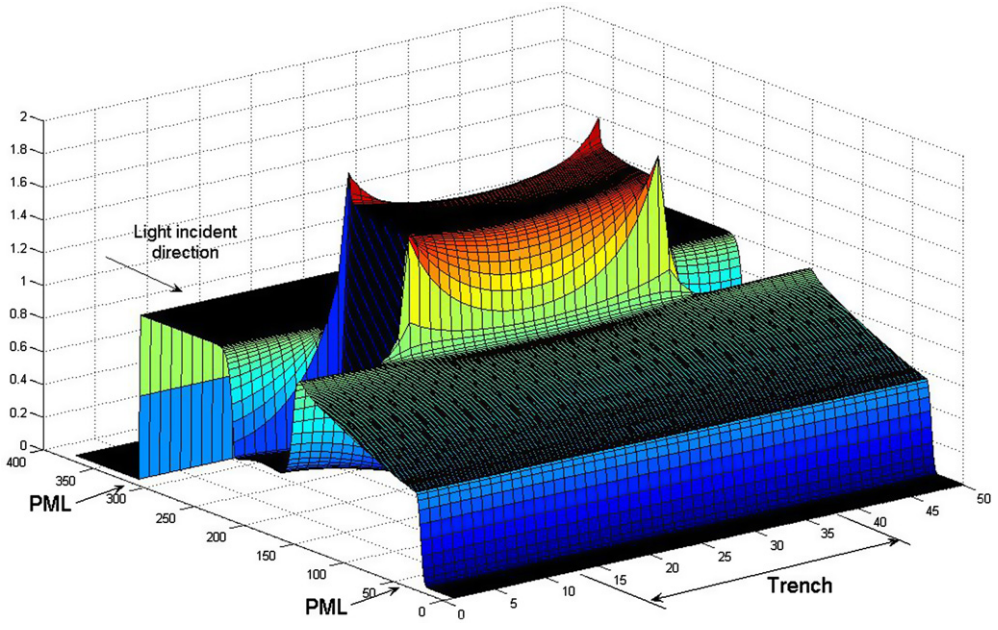


Fig. 8. Poynting vector magnitude distribution of case A3-5 for TM wave at $\lambda = 800$ nm and $\theta = 0°$ with a mesh size of 2 nm.

shows that the absorptance calculated by EMT is in agreement with FDTD except for some small differences at short wavelengths. The agreement is expected due to the small gate and period sizes. Even though the penetration depth might be smaller than the gate height 100 nm at small wavelength, it is comparable to the gate size, and the neighboring medium of the gate is air, which makes it easy for incident light to diffract into the space between gates. This tends to reduce the error of EMT. Fig. 10b shows the absorptance with smaller $l_G/l_P$ and larger $l_P$. While the

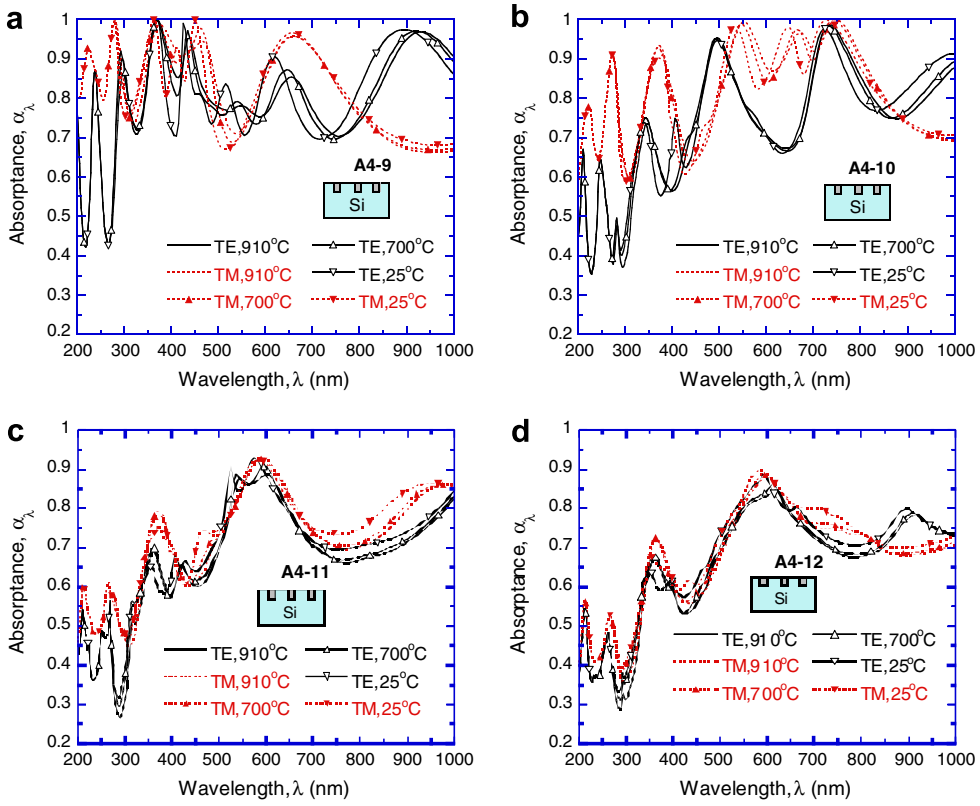


Fig. 9. Absorptance predicted by FDTD for A4 cases at $\theta = 0°$ and $l_T/l_P = 0.8$. (a) $l_T = 160$ nm, $l_P = 200$ nm; (b) $l_T = 320$ nm, $l_P = 400$ nm; (c) $l_T = 640$ nm, $l_P = 800$ nm; (d) $l_T = 1280$ nm, $l_P = 1600$ nm.

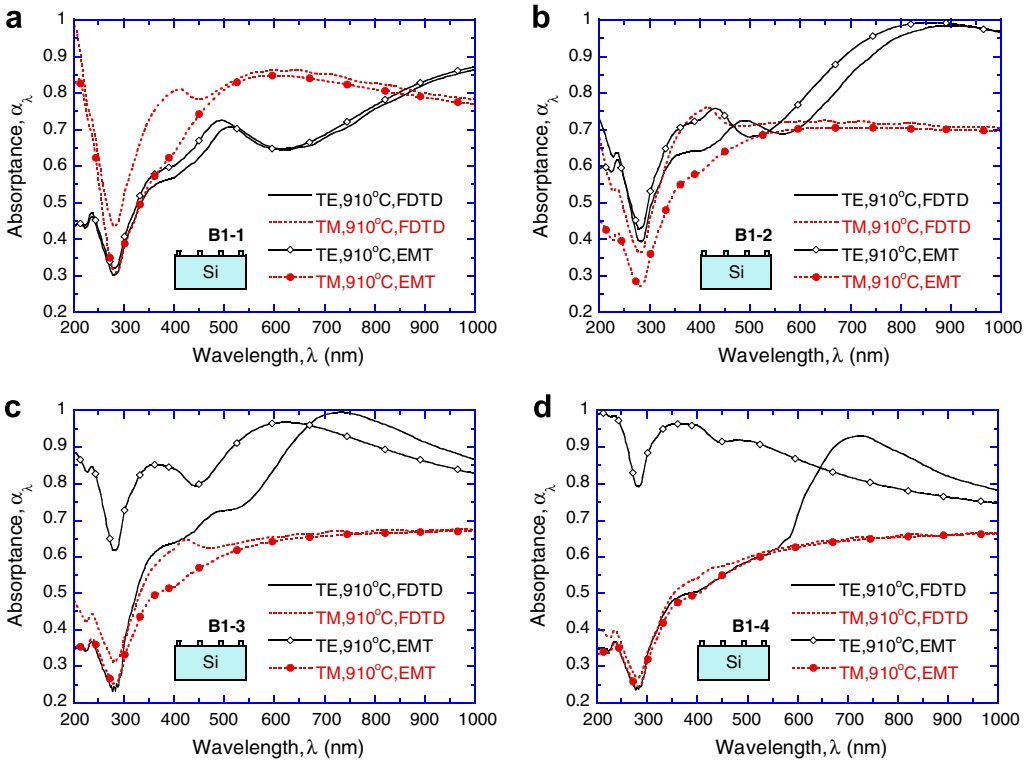


Fig. 10. Absorptance spectra for B1 cases at $\theta = 0°$ and $l_G = 30$ nm. (a) $l_P = 60$ nm, $l_G/l_P = 0.5$; (b) $l_P = 120$ nm, $l_G/l_P = 0.25$; (c) $l_P = 300$ nm, $l_G/l_P = 0.1$; (d) $l_P = 600$ nm, $l_G/l_P = 0.05$.

EMT results still gives a good agreement, the error at short wavelengths increases. With the increase of period and decrease of $l_G/l_P$ ratio, both EMT and FDTD results for TM mode approach to pure silicon since the grating effect diminishes. However, the error of EMT results for TE mode becomes considerable, as shown in Fig. 10c and d. The error is caused by the limitation of EMT, which requires the period to be significantly smaller than the wavelength.

To understand how the gate height influences the overall grating TE absorptance, several gate heights are selected: 20 nm, 40 nm, 60 nm, and 80 nm. The other dimensions are based on case B1-2. Since EMT works well in this structure size, the EMT-computed absorptance for different gate height is shown in Fig. 11. In the figure, when gate height is 20 nm, the absorptance curve is close to that of pure silicon. However, when the height increases to 40 nm or above, the gate height significantly changes the absorptance curve. This shows a slight increase in the gate height can drastically increase the absorptance or produce the equivalent effect of anti-reflection coating. The increased gate height shifts the peak absorptance to longer wavelength due to the increase of optical path length in the effective thin film. According to Airy's formulas, the thin film transmission coefficient $t$ is obtained as

$$t = \frac{t_{12}t_{23}e^{-i\gamma}}{1 + r_{12}r_{23}e^{-2i\gamma}} \tag{16}$$

where $r_{12}$ and $r_{23}$ are the Fresnel reflection coefficients from medium 1 to 2 and medium 2 to 3, respectively. $t_{12}$ and $t_{23}$ are the Fresnel transmission coefficients and $\gamma$ is defined as

$$\gamma = \frac{2\pi}{\lambda} n_2 d \cos\theta_2 \tag{17}$$

where $n_2$ is the refractive index of the thin film, $\theta_2$ is the angle of refraction inside the thin film and $d$ is the thickness. For the cases in Fig. 11, thin film layer is the effective medium, $\theta_2 = 0$. If we further assume that the refractive index of Si is $4.0 + 0i$ at wavelengths longer than 500 nm, $n_2$ can be calculated from Eq. (15), and for case B1-2 it is equal to 2.33. Thus we have $0 < t_{12}t_{23} < 1$ and $0 < r_{12}r_{23} < 1$, and when $\gamma = \pi/2$, $|t|$ reaches the maximum value, which corresponds to $\lambda = 704$ nm for $d = 80$ nm, and $\lambda = 528$ nm for $d = 60$ nm, which match the results in Fig. 11.

Note that the cavity size is only 90 nm for case B1-2, which limits the resonance cavity effect at wavelength below 180 nm, as the resonance cavity wavelength $\lambda_{lmn}$ are determined by [23,24]

$$\lambda_{lmn} = \frac{2}{\sqrt{(l/L_x)^2 + (m/L_y)^2 + (n/2L_z)^2}} \tag{18}$$

where $l$, $m$, and $n$ are integers, $L_x$, $L_y$, and $L_z$ denote the cavity size. In this study, B1 cases have $L_y \to \infty$. Since the wavelength of interest in this study is above 200 nm, which is greater than the upper wavelength limit of the resonant cavity, therefore, the resonance cavity effect can be excluded in the B1 cases.

As discussed earlier, EMT fails to approximate the TE absorptance in Fig. 10c and d, and the cavity widths and heights exclude the resonance cavity effect in these cases. To explain these absorptance curves for TE wave, two more B1 cases are plotted for comparison in Fig. 12. It is noted that the TE absorptance curve separates from that of plain Si at the wavelength equals to the grating period. As the gate can interact with its neighboring region by diffraction, when the wavelength is small and consequently diffraction effects are weak, the affected region is very limited. In this situation the effective medium theory is not

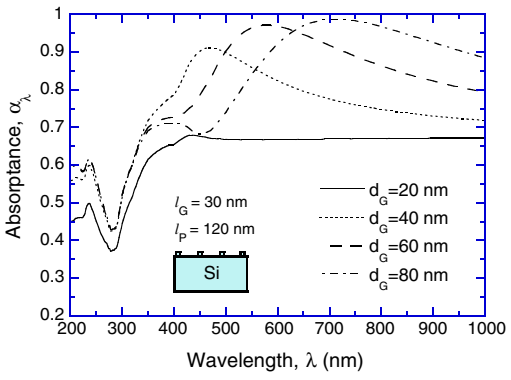


Fig. 11. The TE wave absorptance calculated by EMT for B1-2 base case at $\theta = 0°$ with different gate heights.

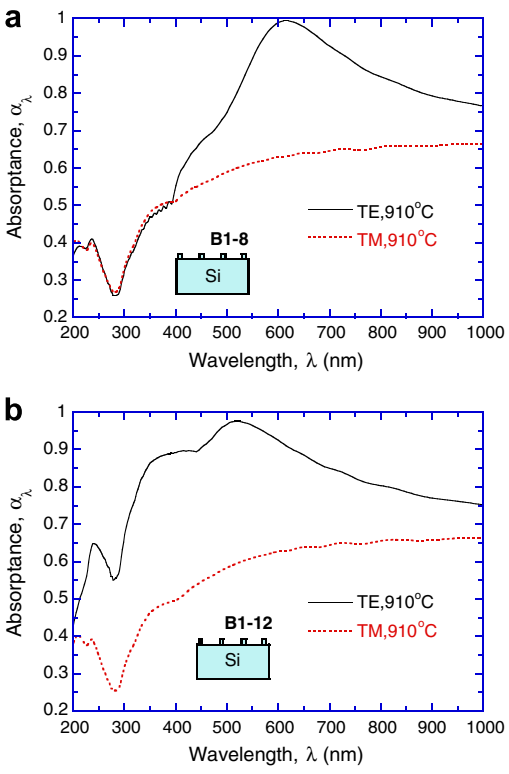


Fig. 12. Absorptance predicted by FDTD for B1 cases at $\theta = 0°$ and $l_G/l_P = 0.05$. (a) $l_G = 20$ nm, $l_P = 400$ nm; (b) $l_G = 10$ nm, $l_P = 200$ nm.

reliable [25]. The absorptance is close to that of the plain Si. It is only when the wavelength increases to the grating period, then the affected region covers the whole grating structure and the gate size relative to wavelength is small enough to have strong diffraction, which then causes absorptance to deviate from that of pure Si. In this case, the combined gate and vacuum space starts to emulate the mixture concept implied in the EMT. When wavelength increases further, e.g., above 1000 nm in Fig. 10d, the EMT prediction approaches the FDTD result.

### 3.3. Directional dependence

Fig. 13 shows the TE and TM wave spectral-directional absorptance of structures A3-3, A3-5, and A3-9, modeled by RCWA. Different wavelengths are selected to show the absorptance in ultraviolet, visible, and near-infrared regions. Since the filling ratio of 0.1 for A3-3 structure is small, the absorptance is close to that of plain Si. The absorptance for the TE wave decreases monotonically while the absorptance for the TM wave increases with incidence angle up to the Brewster angle or the principal angle. The TM wave absorptance reaches 1.0 at the Brewster angle when $\kappa$ of silicon is close to zero and $n$ is 4.3 and 3.95 at the wavelength of 600 nm and 800 nm, respectively. On the other hand, the peak absorptance at 200 nm, at which $\kappa$ is 2.9 and $n$ is 1.0 for silicon, is less than 0.7 at the principal angle. Although $\kappa$ is 2.35, the absorptance peak at wavelength of 400 nm does not decrease too much due to the large $n$ value of 5.1 at this wavelength. When the

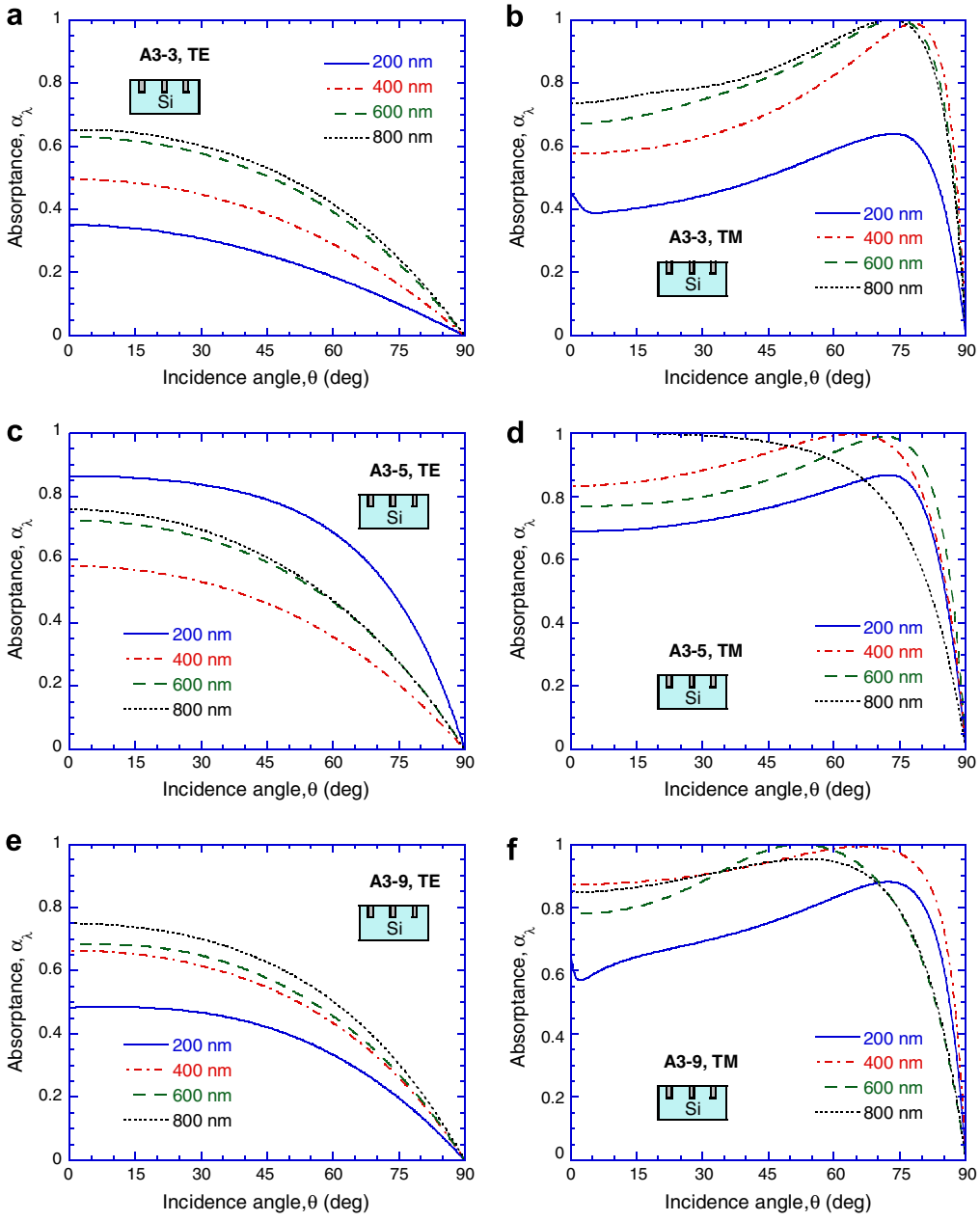


Fig. 13. Effect of the angle of incidence on the absorptance of A3-3, A3-5, and A3-9.

incidence angle is close to zero, the absorptance spectrum at 200 nm for the TM wave shows an abrupt change due to Wood's anomaly [24]. For the structure period of 200 nm, Wood's anomaly can only appear at normal incidence for $\lambda = 200$ nm.

Fig. 13c and d shows the absorptance of A3-5 (AT3-5) structures with a period of 100 nm and a trench filling ratio of 0.5. The absorptance increases at all four wavelengths, especially at 200 nm. Such a large increase should come from the anti-reflection effect. Furthermore, the absorptance at 800 nm at normal incidence is close to 1.0, decreasing gradually without an absorptance peak. The absorptance in Fig. 6a has similar maximum absorptance at normal incidence, which may arise from the cavity resonance effect [23,26,27]. The TM wave absorptance at other wavelengths also increases and shows a peak but the incidence angles corresponding to the peaks vary with wavelengths and structures. Fig. 13e and f shows the absorptance of A3-9 (AT3-9) structures with a period of 200 nm and a trench filling ratio of 0.5. Since the structure period is the same as that of A3-3, Wood's anomaly also shows up for the TM wave. Furthermore, the TE wave absorptance at 200 nm is the smallest among all wavelengths considered. The anti-reflection effect also increases the absorptance at all wavelengths. However, due to the difference in the period, the TE wave absorptance of A3-9 at 200, 600, and 800 nm is lower than those of A3-5 but is higher at 400 nm. On the other hand, the TM wave absorptance spectra at the 400, 600, and 800 nm wavelengths are very close to one another.

Fig. 14 shows the absorptance for structures of B1-3 and B1-9 modeled by RCWA. For B1-3, even with a very small gate filling ratio is 0.1 and a relatively thin gate of 100 nm, the absorptance spectra changes considerably with respect to that for plain Si. For example, the TE wave absorptance at $\lambda = 600$ and 800 nm can exceed 0.8, and the absorptance at 200 nm shows a peak at the incidence angle of 50.5°. Moreover, the peak absorptance at 200 nm has the highest value and the effect of principle angles at $\lambda = 200$, 600, and 800 nm are not obvious. On the other hand, Wood's anomaly appears at $\lambda = 200$ and 400 nm when the incidence angle is 19.5°. Here, the anomaly shows up for both the TE and TM wave incidence, and the absorptance can either increase or decrease with the incidence angle at the anomaly. Fig. 14c and d shows the absorptance of B1-9 with a gate filling ratio of 0.5 and a period of 20 nm. The absorptance for the TE wave increases compared to that of plain Si. On the other hand, the TM wave absorptance increases at the angle close to normal incidence but the absorptance peak at the Brewster angle disappears, except at the 400 nm wavelength. Such absorptance enhancement at normal incidence may come from the anti-reflection coating effect as well.

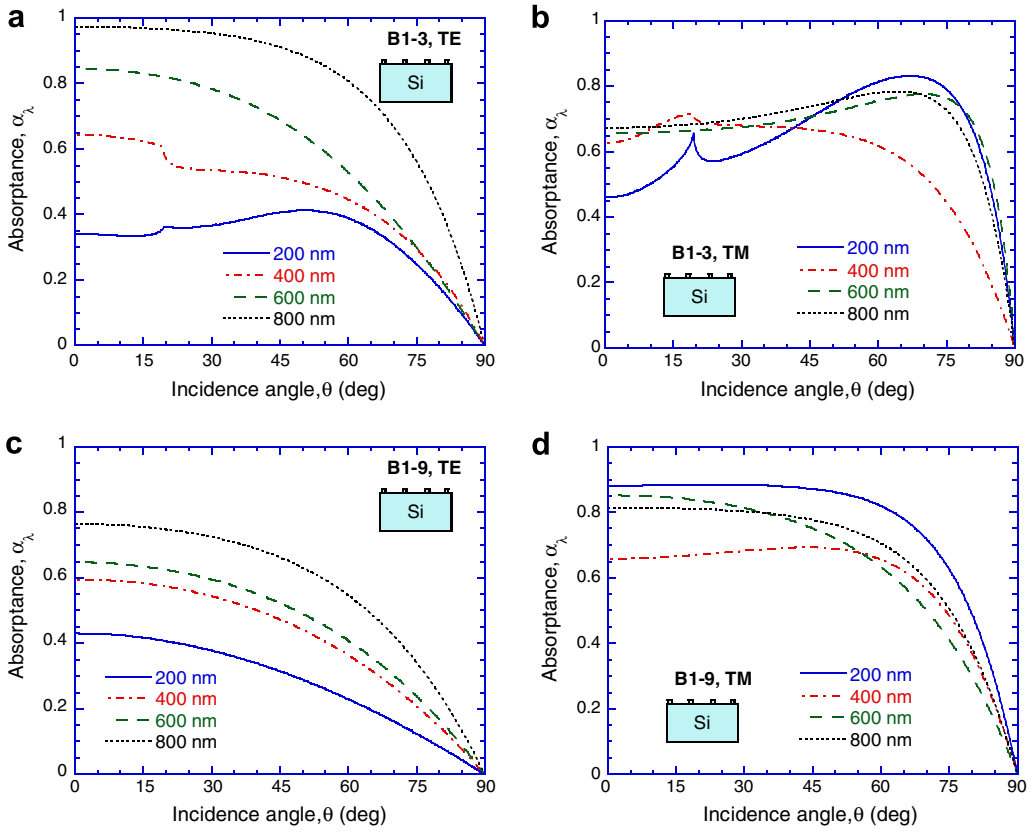


Fig. 14. Effect of the angle of incidence on the absorptance B1-3 and B1-9.

## 4. Conclusions

An extensive numerical study of the absorptance of the wafer front side with parametric variation of gate and trench sizes is presented. The wavelength range of interest, 200–1000 nm, covers the radiation heat sources of flash-lamp arc and some pulsed laser annealing approaches. Two rigorous methods, the finite-difference time-domain method and rigorous coupled-wave analysis, and one approximate model, the effective medium theory, are used to solve the electromagnetic wave propagation in nanometer scale device structures. It is found that at small filling ratios and small periods (subwavelength gratings) the effective medium theory can describe the spectral variation reasonably well, especially for the transverse electric wave. In the cases with trench size variation (A3 group), the resonance cavity effect may increase the absorptance as the trench width increases. Additionally, the interference of the substrate reflection and trench reflection produces oscillations in the absorptance spectrum. This is an effect that is distinct from the typical thin film interference phenomena. In the cases with trench size increases at several different filling ratios (A4 group), the absorptance does not change much at small filling ratio, even though the trench width increases from 10 to 80 nm. However, more significant variation in the absorptance is observed at large filling ratio (0.8). The peak absorptance in the cases with varying gate size (B1 group) can be attributed to the thin film effect. The directional-hemispherical absorptance with gates on top of Si substrate shows Wood's anomaly. It is also found that the principle angle for TM waves is sometimes not obvious or corresponds to the normal incidence, even at long wavelengths. This work improves the understanding of the geometrical effects of device features on the radiative properties, which is important for optimization of advanced annealing techniques in semiconductor manufacturing.

## Acknowledgement

The National Science Foundation supported the work Grants CTS-0331153 at the Florida Institute of Technology and CTS-0500113 at the Georgia Institute of Technology.

## References

[1] Semiconductor Industry Association, International Technology Roadmap for Semiconductors 2004. Update: <http://public.itrs.net>, 2004.
[2] W. Lerch, S. Paul, J. Niess, S. McCoy, T. Selinger, J. Gelpey, F. Cristiano, F. Severac, M. Gavelle, S. Boninelli, P. Pichler, D. Bolze, Advanced activation of ultra-shallow junctions using flash-assisted RTP, Mat. Sci. Eng. B 124–125 (2005) 24–31.
[3] G.G. Bentini, L. Correra, Analysis of thermal stresses induced in silicon during xenon arc lamp flash annealing, J. Appl. Phys. 54 (1983) 2057–2062.
[4] Y.-B. Chen, Z.M. Zhang, P. Timans, Radiative properties of patterned wafers with nanoscale linewidth, J. Heat Transfer 129 (2007) 79–90.
[5] Z.M. Zhang, C.J. Fu, Q.Z. Zhu, Optical and thermal radiative properties of semiconductors related to micro/nanotechnology, Adv. Heat Transfer 37 (2003) 179–296.
[6] M.G. Moharam, D.A. Pommet, E.B. Grann, T.K. Gaylord, Stable implementation of the rigorous coupled-wave analysis for surface-relief gratings: enhanced transmittance matrix approach, J. Opt. Soc. Am. A 12 (1995) 1077–1086.
[7] M.G. Moharam, E.B. Grann, D.A. Pommet, T.K. Gaylord, Formulation for stable and efficient implementation of the rigorous coupled-wave analysis of binary gratings, J. Opt. Soc. Am. A 12 (1995) 1068–1076.
[8] L.F. Li, Use of Fourier series in the analysis of discontinuous periodic structures, J. Opt. Soc. Am. A 13 (1996) 1870–1876.
[9] M. Auslender, S. Hava, Zero infrared reflectance anomaly in doped silicon lamellar gratings. I. From antireflection to total absorption, Infrared Phys. Technol. 36 (1995) 1077–1088.
[10] K. Fu, P.-f. Hsu, Radiative properties of gold surfaces with one-dimensional microscale Gaussian random roughness, Int. J. Thermophys. 28 (2) (2007) 598–615.
[11] D.H. Raguin, G.M. Morris, Antireflection structured surfaces for the infrared spectral region, Appl. Opt. 32 (1993) 1154–1167.
[12] A. Sentenac, J.-J. Greffet, Design of surface microrelief with selective radiative properties, Int. J. Heat Mass Transfer 37 (1994) 553–558.
[13] P. Lalanne, D. Lemercier-Lalanne, Depth dependence of the effective properties of subwavelength gratings, J. Opt. Soc. Am. A 14 (1997) 450–458.
[14] A.F. Erofeev, A.V. Kolpakov, T.M. Makhviladze, A.V. Martjushenko, A.V. Panjukhin, O.S. Volchek, M. Orlowski, Comprehensive RTP modelling and simulation, in: Proceedings of the 3rd International Rapid Thermal Processing Conference 181–197, IEEE, 1995.
[15] J.P. Hebb, K.F. Jensen, The effect of patterns on thermal stress during rapid thermal processing of silicon wafers, IEEE Trans. Semi. Manu. 11 (1998) 99–107.
[16] H. Tada, A.R. Abramson, S.E. Mann, I.N. Miaoulis, P.Y. Wong, Evaluating the effects of thin film patterns on the temperature distribution of silicon wafers during radiant processing, Opt. Eng. 39 (2000) 2296–2304.
[17] J. Liu, S.J. Zhang, Y.S. Chen, Rigorous electromagnetic modeling of radiative interactions with microstructures using the finite volume time-domain method, Int. J. Thermophys. 25 (2004) 1281–1297.
[18] A. Taflove, S.C. Hagness, Computational Electrodynamics: The Finite-Difference Time-Domain Method, third ed., Artech House, Boston, MA, 2005, Chapter 3.
[19] K. Fu, P.-f. Hsu, Modeling the radiative properties of microscale random roughness surfaces, J. Heat Transfer 129 (2007) 71–78.
[20] G.E. Jellison Jr., F.A. Modine, Optical functions of silicon between 1.7 and 4.7 eV at elevated temperatures, Phys. Rev. B 27 (1983) 7466–7472.
[21] S.M. Rytov, Electromagnetic properties of a finely stratified medium, Sov. Phys. JETP 2 (1956) 466–475.
[22] M. Born, E. Wolf, Principles of Optics, seventh ed., Cambridge University Press, Cambridge, UK, 1999, Chapter 1.
[23] H. Sai, H. Yugami, Thermophotovoltaic generation with selective radiators based on tungsten surface gratings, Appl. Phys. Lett. 85 (2004) 3399–3401.
[24] A. Hessel, A.A. Oliner, A New Theory of Wood's Anomalies on Optical Gratings, Appl. Opt. 4 (1965) 1275–1297.
[25] F. Ghmari, T. Ghbara, M. Laroche, R. Carminati, J.-J. Greffet, Influence of microroughness on emissivity, J. Appl. Phys. 96 (5) (2004) 2656–2664.
[26] S. Maruyama, T. Kashiwa, H. Yugami, Thermal radiation from two-dimensionally confined modes in microcavities, Appl. Phys. Lett. 79 (2001) 1393–1395.
[27] P.J. Hesketh, J.N. Zemel, B. Gebhart, Organ pipe radiant modes of periodic micromachined silicon surfaces, Nature (London) 324 (1986) 549–551.